Faraday Discussions

Cite this: DOI: 10.1039/d5fd00167f

ROYAL SOCIETY OF CHEMISTRY

PAPER

View Article Online
View Journal

Structure-controlled sulfur poisoning and hydrogen-induced regeneration in single Pd nanoparticles probed by nanospectroscopy

Mazal Kostan-Carmiel,[a] Yehonatan Hovav,[a] Athanasios Theodoridis,[b] Christoph Langhammer[b] and Elad Gross *[a]

Received 15th December 2025, Accepted 3rd February 2026
DOI: 10.1039/d5fd00167f

Structural order and surface crystallinity of palladium nanoparticles (Pd NPs) significantly affect their chemical and mechanical stability, and impact their resistance to poisoning and efficiency in hydrogen (H_2) (de)sorption. This study investigates the impact of sulfuric acid (H_2SO_4) poisoning on pristine and annealed Pd NPs to identify the influence of structure on the density and stability of poisoners. Electron microscopy and diffraction analyses show that annealing transforms initially amorphous, rough, and aggregated particles into spherical and crystalline NPs with better-defined grain boundaries. Nanoscale AFM-IR analysis shows that pristine NPs rapidly decompose SO_x upon H_2 exposure, and SO_x is mainly located on the rim of the NP. Annealed NPs maintain stable, localized SO_x signatures across multiple N_2–H_2 cycles, and only after the second H_2 exposure cycle the SO_x is removed from the central part of the NP. Contact potential difference analysis shows the strong affinity of SO_x to the rim of the NP. Together, these results reveal that crystallinity and defect density dictate both the spatial distribution and chemical stability of sulfur species on Pd surfaces. Pristine, defect-rich NPs promote rapid H_2-induced SO_x reduction and selective desorption from their centers, whereas annealed, crystalline NPs stabilize SO_x more strongly and exhibit delayed desorption. This direct link between structural order, SO_x binding strength, and hydrogen (de)sorption affinity underscores the critical role of nanoscale morphology in controlling poisoning dynamics and highlights nanospectroscopy as a powerful tool for correlating local structure with chemical functionality.

Introduction

Catalytic behavior of metallic nanoparticles (NPs) is influenced by their atomic arrangement, degree of crystallinity, and distribution of structural defects.[1–3]

[a]Institute of Chemistry, and the Center for Nanoscience and Nanotechnology, The Hebrew University, Jerusalem 91904, Israel. E-mail: elad.gross@mail.huji.ac.il
[b]Department of Physics, Chalmers University of Technology, Gothenburg 412 96, Sweden

Grain size, surface roughness, facet orientation, and defect density all contribute to shaping the electronic structure and adsorption energetics of active sites, thereby governing reaction pathways and catalytic efficiency.[4–9] Structural imperfections provide highly reactive adsorption sites, including disordered atomic domains, vacancies, steps, and grain boundaries. However, these imperfections can also contribute to mechanical deformation, chemical restructuring, and long-term degradation of the material.[10] Therefore, rational design of catalytic materials requires a clear understanding of the interplay between structural order and chemical functionality.[11–13]

There has been extensive research demonstrating the influence of structure on catalytic performance across a variety of metallic systems. Amorphous or defect-rich materials often exhibit enhanced initial reactivity due to the presence of a high density of reactive surface sites, but may suffer from limited stability or irreversible restructuring.[14,15] In contrast, crystalline NPs with well-defined facets provide more predictable adsorption behavior and improved stability.[16–19] Small or irregular NPs often exhibit rapid adsorption kinetics, but experience high lattice strain after repeated reaction exposure, while larger or more faceted particles possess greater mechanical stability.[20,21] It can be therefore deduced that crystallinity, morphology, and defect density have a crucial impact on the catalytic performance and stability of materials.

Catalyst stability is strongly affected by the susceptibility to surface poisoning. Molecules such as CO, NO_x, H_2O, and sulfur-oxide species (SO_x) can deactivate surface sites, due to strong interaction with the metal surface, preventing reactant adsorption and its activation.[10,22–24] The poisoning mechanism is highly sensitive to the surface structure. Surfaces with a high density of adsorption sites can facilitate strong, sometimes irreversible binding of poisoning species.[25,26] Consequently, the role and reversibility of catalyst poisoning depend on both the chemical nature of the poisoner and the structural characteristics of the active surface.

Pd NPs are ideal materials for studying structure–function relationships due to their exceptional ability to dissociate and absorb hydrogen. Hydrogen uptake in Pd induces a reversible phase transition accompanied by lattice expansion, making Pd a powerful system for hydrogen storage, catalysis, and sensing.[9,22,27–30] However, the reversibility and kinetics of phase transition depend strongly on structural and morphological characteristics of Pd NPs, including size, crystallinity, and surface defect density. Amorphous domains, rough surfaces, and high density of surface defects are common features in pristine Pd NPs, which enhance their hydrogen sorption rates, but also induce irreversible lattice strain upon repeated cycling.[30,31] Alternatively, thermal annealing can be used to transform amorphous Pd NPs into polycrystalline nanostructures that are characterized with smooth surfaces and lower defect density. This structural change does not only enhance the particle uniformity but also leads to more predictable and reversible phase transitions during hydrogen (de)sorption cycling.[30,32,33] Therefore, structural order is directly related to mechanical robustness, phase-transition reversibility, and hydrogen reactivity in Pd-based nanomaterials.[34–37]

Pd surfaces are highly vulnerable to poisoning, and specifically to sulfur poisoning.[9,38,39] SO_x species bind strongly to Pd, blocking H_2 dissociation sites and significantly reducing their catalytic activity.[9] Defect-rich, pristine Pd NPs provide a significant number of high-energy adsorption sites, which result in rapid SO_x

accumulation and accelerated deactivation. Annealed Pd NPs, on the other hand, exhibit a lower defect density and well-defined crystallographic facets, resulting in a higher resistance to sulfur adsorption as well as a better recovery following H_2 exposure.[40]

Due to their structural complexity, which induces both inter- and intra-particle variances, a comprehensive understanding of structure–reactivity correlations in Pd NPs requires an in-depth nanoscale analysis.[41–43] Such analysis will enable spatial mapping of poisoners' distribution and reveal how variations in surface coordination influence the adsorption strength, stability and diffusivity of sulfur-based species. Recent advances in high spatial resolution spectroscopy have enabled nanoscale investigations of catalytic nanoparticles.[7,8,44–54] In particular, infrared (IR) nanospectroscopy measurements[55,56] have shown that the types and adsorption geometries of SO_x species vary significantly due to morphological and structural heterogeneity among individual nanoparticles.[9,39] However, the connection between crystallinity, location-dependent SO_x adsorption (rim *vs.* center), and the kinetics of H_2-induced SO_x reduction remains insufficiently resolved.

Herein, we combine AFM-IR, KPFM, and electron microscopy to correlate the structural evolution of pristine *versus* annealed Pd NPs with their sulfur-poisoning behavior. We show that annealing transforms amorphous, highly corrugated particles into crystalline nanostructures with smoother surfaces, which in turn stabilizes SO_x species and delays their H_2-induced desorption. In contrast, pristine NPs exhibit rapid SO_x reduction and selective desorption from their central regions, with preferential retention at defect-rich rim sites. These insights establish a direct structure–poisoning relationship and highlight how crystallinity governs both SO_x stability and hydrogen (de)sorption dynamics.

Experimental

Nanofabrication of Pd NPs samples

Pd nanodisk arrays were fabricated on 1 cm × 1 cm fused silica substrates using Hole-mask Colloidal Lithography (HCL).[57] The particles had a nominal size of 210 nm (diameter) and 25 nm (height), covering approx. 10% of the total sample area. For the annealed NPs, subsequent annealing was performed at 500 °C for 18 h under a flow of 2 vol% H_2 in Ar.

AFM-IR and KPFM measurements

Atomic force microscopy infrared (AFM-IR) and Kelvin probe force microscopy (KPFM) measurements were performed in tapping mode using a nanoIR-3 setup (Anasys, Bruker). AFM-IR setup is equipped with a Bruker Hyperspectral Quantum Cascade Lasers (QCL) laser source (790–1950 cm^{-1}), a gold-coated Si probe with a nominal diameter of ~25 nm, resonance frequencies of 75 ± 15 kHz, and spring constants of 1–7 N m^{-1}. Spectra were acquired with an average integration time of 5 s per spectrum and a spectral resolution of 2 cm^{-1}. For each measurement point, IR spectra were obtained by averaging five consecutive spectra collected at the same location on the nanoparticle. KPFM measurements were performed using a Pt/Ir probe with a nominal diameter of ~25 nm, resonance frequency of 62 ± 14 kHz, and spring constants of 1–6 N m^{-1}. Nano-IR measurements were

conducted *in situ* at room temperature under exposure to varying gas environments (1 atm of N_2 or 1 atm of 100 : 1 N_2 : H_2 for 60 minutes), with humidity values less than 10%.

H_2SO_4 poisoning

Sulfur poisoning of Pd NPs was performed by immersing the sample in a 10 mM aqueous H_2SO_4 solution for 10 min at 25 °C. Following exposure, the sample was dried on a hot plate in air at 100–110 °C for 10 min to remove physisorbed surface residues. The poisoning conditions were selected based on previous studies demonstrating that these conditions preserve the structure of both the Pd nanoparticles and the substrate, while harsher conditions induce structural changes.[39]

FIB-TEM measurements

A lamella of Pd NPs for Scanning Transmission Electron Microscopy (STEM) imaging was prepared using a Focused-Ion Beam (FIB) (Helios NanoLab 460F1). STEM images were taken using an aberration probe-corrected Themis Z-G3 (Thermo Fisher Scientific) operated at 300 kV, equipped with an Annular Dark Field Detector (HAADF) for the diffraction pattern of a single Pd NP.

Results and discussion

Pd NPs were prepared on a Si (100) wafer with a native oxide layer by using Hole-mask Colloidal Lithography nanofabrication. In order to prepare NPs that are characterized with a better-defined structure, the NPs were annealed to 500 °C for 18 h under a flow of 2% v/v H_2 in Ar. The chosen annealing temperature is above the Hüttig temperature (0.3 T_m, T_m = melting temperature of Pd = 1828 K) of Pd (275 °C) and below the Tammann temperature (0.5 T_m, ~650 °C) and thus leads to surface atom diffusion and smoothing without sintering of nanoparticles due to ripening and migration. High-resolution TEM (HR-TEM) imaging shows the

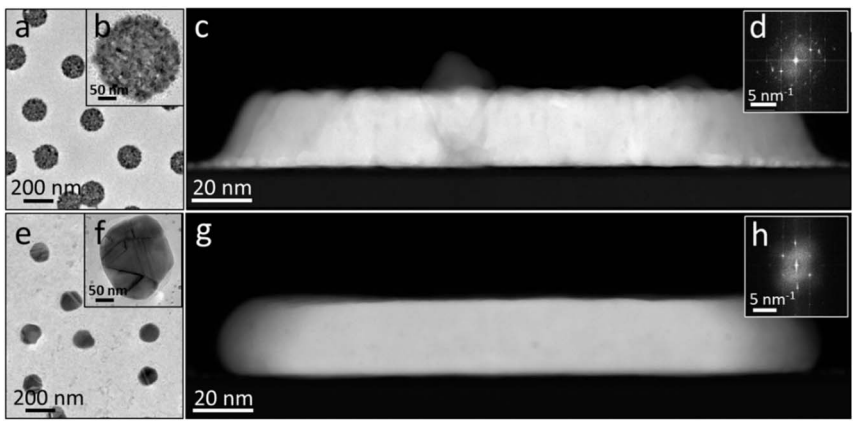

Fig. 1 TEM (a and e), HR-TEM (b and f), FIB-TEM cross-sectional images (c and g) and FFT diffraction patterns (d and h) of pristine and annealed Pd NPs, respectively.

morphology and structure of the pristine and annealed Pd NPs (Fig. 1a, b, e and f, respectively).

Characterization was conducted by using FIB to extract a lamella and its analysis by TEM imaging and fast Fourier transform (FFT) of the diffraction pattern of the pristine and annealed NPs (Fig. 1c, d, g and h, respectively).

Both samples included NPs with a diameter and height of 190 ± 10 nm and 25 ± 5 nm, respectively. It was also identified that the pristine NPs are characterized with a more corrugated surface that is constructed of nanoscale aggregates (Fig. 1a and b). The annealed NPs showed a more spherical morphology with smoother surfaces, better-defined particle boundaries, and enhanced crystallinity (Fig. 1e and f), which are consistent with thermally driven intra-particle sintering and grain growth.

TEM cross-sections of the pristine NP revealed a largely amorphous structure, as indicated by the diffuse, disordered FFT patterns (Fig. 1c and d). Conversely, annealed NPs displayed a different morphology, while the TEM cross-sections revealed sharply defined crystalline domains, and the corresponding FFT images exhibited a distinct diffraction pattern that is consistent with a well-ordered face-centered cubic (FCC) structure (Fig. 1g and h). These results confirm that thermal annealing promotes the transformation of disordered Pd NPs into nanostructures that are more robust, with defined crystalline domains and lower density of grain boundaries.

The pristine and annealed NPs were immersed in H_2SO_4 (10 mM, 25 °C, 10 minutes), followed by heating the dried sample in air (110 °C, 10 minutes) to remove physisorbed residues. Localized IR spectra were acquired from the center of the pristine and annealed NPs (Fig. 2a and b, respectively). The pristine NP exhibited characteristic IR absorption bands (Fig. 2a, blue colored spectrum) at 1100, 1194 and 1228 cm^{-1}. The feature at 1100 cm^{-1} was assigned to sulfates adsorbed with 3-fold geometry on metallic sites (Pd^0) of Pd(111) facets, while the peak at 1194 cm^{-1} is attributed to sulfates adsorbed with 3-fold geometry with the C_{3v} symmetry on electron-deficient Pd_x^+ sites.[58] The peak at 1228 cm^{-1} is attributed to SO_2 species.[59] The peak at 1451 cm^{-1} was assigned to 2-fold or 3-fold sulfates adsorbed on oxidized Pd sites (*i.e.*, Pd_x^+). The annealed NP (Fig. 2b, blue colored spectrum) showed signals at 1048 and 1095 cm^{-1}, correlated to

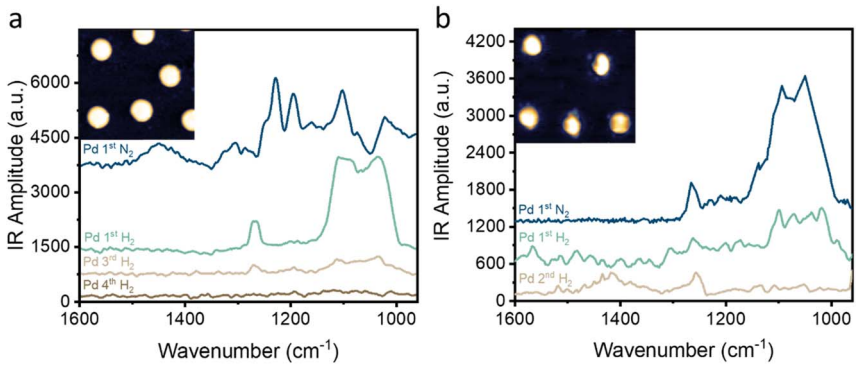

Fig. 2 IR nanospectroscopy measurements acquired on the center of pristine (a) and annealed (b) NPs after their exposure to H_2SO_4. IR spectra were acquired following exposure to cycles of N_2 and H_2.

symmetric and asymmetric S–O stretching of sulfate, respectively, while the minor signal at 1264 cm^{-1} was correlated to SO_2. The detection of a broad absorbance band at 1000–1150 cm^{-1} with a split to two peaks is correlated to sulfate adsorption in a bidentate adsorption mode with C_{2V} symmetry.[58]

After exposure to H_2 the IR signal of the pristine sample (Fig. 2a, green-colored spectrum) was similar to that of the annealed sample, with two dominant peaks at 1035 and 1108 cm^{-1} and a smaller peak at 1267 cm^{-1}. The disappearance of the peaks at 1228 cm^{-1}, coupled with the presence of a new peak at 1267 cm^{-1}, was assigned to structural changes that modified the adsorption geometry.[60] Consecutive H_2–N_2 cycles led to an overall decrease in the SO_x signal and after 3 cycles only a minor signature was detected on the pristine NP. No signal was detected on the central part of the NPs after the 4th cycle, indicative of SO_x desorption from the center of the NP (Fig. 2a, brown-colored spectrum).

Exposure to H_2 reduced the vibrational signals on the annealed NP to about 1/3 of their initial amplitude. After exposure to a second cycle of H_2, the IR signals in the 1000–1100 cm^{-1} range were not detected. The peak at 1264 cm^{-1} was attributed to SO_2 species.[59] The peak at 1420 cm^{-1} was assigned to 2-fold or 3-fold sulfates adsorbed on oxidized Pd sites (*i.e.*, Pd_x^+). It can be concluded that exposure to H_2SO_4 led to the formation of different surface chemistry on the pristine and annealed NPs.

Quantitative analysis of surface roughness was performed based on AFM measurements (Fig. 3). The pristine NPs exhibited an average surface roughness of 3.12 ± 0.17 nm, which increased to 3.40 ± 0.10 nm after exposure to H_2SO_4 (Fig. 3, black colored curves). Following two cycles of exposure to N_2 and H_2 the roughness value decreased to 3.25 ± 0.08 nm. The annealed Pd NPs displayed a smoother surface, with an overall roughness of 1.92 ± 0.29 nm before exposure to H_2SO_4, which decreased to 1.24 ± 0.20 nm after poisoning. Following two cycles of exposure to N_2 and H_2 the roughness values of both the pristine and annealed samples showed a moderate decrease. It was previously demonstrated by us that due to the high structural similarity of the nanoparticles, analysis of five nanoparticles provides statistically meaningful values that are representative of the behavior of the nanoparticle array.[9]

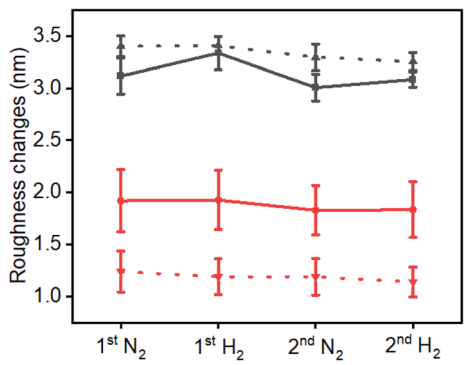

Fig. 3 Average surface roughness of pristine (black) and annealed (red) NPs following sequential N_2–H_2 cycles, shown before (solid lines) and after H_2SO_4 poisoning (dotted lines). Error bars represent the standard deviation across the analyzed particles, based on average of five NPs.

Nanoscale IR mapping was performed to correlate the structural properties with the distribution and stability of poisoners. Nanoscale AFM-IR mapping was performed at 1108 cm^{-1}, correlated to the asymmetric S–O vibration of SO_4^{2-} (Fig. 4a). Quantitative analysis of the variance in the IR amplitude on single NPs was performed by dividing the NP surface into concentric rings and averaging the IR signal across the ring (Fig. 4b). The averaged IR signal of each ring was then plotted as function of the radial distance of the ring from the center of the NP to provide a quantitative analysis of the IR signal amplitude on different sites of the NP (Fig. 4c).

AFM-IR maps were recorded for the pristine and annealed NPs (Fig. 5a and c, respectively) after exposure to H_2SO_4 and following consecutive N_2 and H_2 cycles. Quantitative analysis of the IR signal was performed for two pristine and annealed NPs (Fig. 5b and d, respectively), in a similar approach to the one described in Fig. 4. The pristine NPs showed an AFM-IR signal that covered the NPs, indicating that the NPs are coated with SO_x molecules (Fig. 5a). Analysis of the AFM-IR maps showed similar signals for the central parts of the NPs with a continuous decrease in the IR signal toward the edges of the NPs (Fig. 5b, black-colored curve). Following exposure to H_2, the IR signal in the central part of the pristine NPs decreased and a ring of IR signal was detected on the outer rim of the NP (Fig. 5a). This was also validated by analysis of the IR signals (red-colored curve, Fig. 5b). A second exposure cycle to N_2 (blue-colored curve, Fig. 5b) and to H_2 (green-colored curve, Fig. 5b) led to sharpening of the IR signal toward the rim of the NP. These results show the selective desorption of SO_x from the central part of the NP following exposure to H_2.

A different pattern was detected for the annealed NP. AFM-IR imaging probed the selective desorption of SO_x species only after the second H_2 cycle (Fig. 5c). Quantitative analysis of the IR signal showed that prior to exposure to H_2, the IR signal reached its maximum at the center of the NP and moderately decreased toward the edges of the NP (black colored curve, Fig. 5d). Following H_2 exposure, the maximum IR signal shifted from the centre toward the rim of the NP (red colored curve, Fig. 5d) and this shift further increased after the second H_2 exposure (green colored curve, Fig. 5d).

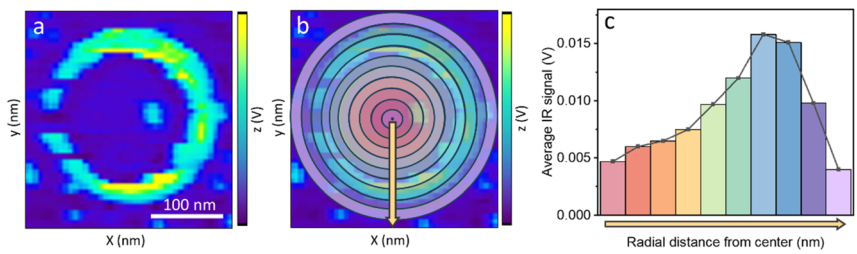

Fig. 4 Quantitative analysis of AFM-IR mapping. (a) AFM-IR mapping of pristine NP following H_2SO_4 poisoning was recorded at 1108 cm^{-1}. (b) Quantitative analysis of the IR signal across the NP surface was performed by dividing the NP into concentric rings, each with a fixed width of ~4.5 pixels (≈3 nm), and calculating the averaged IR signal within each ring. Ten rings are shown as an example in (b). The averaged signal of each ring was then plotted as a function of its distance from the nanoparticle's center of mass (c). The yellow arrow indicates the radial distance measured from the particle's center of mass.

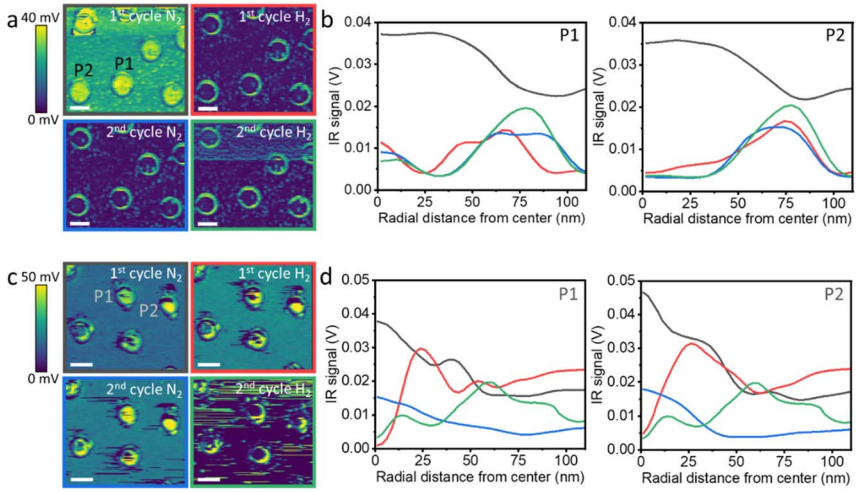

Fig. 5 AFM-IR mapping at 1108 cm^{-1} of pristine (a) and annealed (c) Pd NPs after exposure to H_2SO_4 and following consecutive N_2 and H_2 cycles. The surfaces of two NPs (labeled P1 and P2 in panels a and c) were divided into concentric rings, and the averaged IR signal of each ring was plotted as a function of the radial distance from the particle center. The radial IR signal analyses of the pristine and annealed NPs are shown in panels (b and d), respectively. Data in (b) and (d) are shown after the first exposure to N_2 and H_2 (black and red traces, respectively) and after the second exposure to N_2 and H_2 (blue and green traces, respectively). The scale bar represents 200 nm.

These observations are consistent with the analysis of surface roughness (Fig. 3). Pristine NPs exhibit higher surface corrugation values, and noticeable changes in surface roughness were measured following exposure to H_2, indicating a dynamic and adaptable surface structure. Due to enhanced atomic mobility, SO_x diffusion and desorption occurred during H_2 exposure, presumably due to dissociation of H_2 that enabled the following reduction and desorption of SO_x species. The annealed NPs exhibit smaller and more consistent roughness variations, indicating that the surface is structurally more stable. In addition, it is expected that H_2 dissociation will have higher kinetic barriers on a surface with a lower density of surface defects. Thus, the rate of SO_x reduction, followed by desorption, is expected to be slower on the annealed NPs. For both the pristine and annealed NPs there is higher stability of SO_x on the edge of the NP, correlated with the higher density of surface defects on these sites.

KPFM measurements were performed to probe the changes in contact potential difference (CPD), which reflects the difference in work function between the tip and sample (Fig. 6). As the transformation from metal to metal–hydride is expected to influence the work function value, KPFM measurements can shed light on the hydrogenation of the particle's top layers and the impact of surface poisoning on hydrogen (de)sorption kinetics.

AFM topography and CPD mapping were performed for pristine and annealed NPs before (Fig. 6a and b, respectively) and after (Fig. 6c and d, respectively) exposure to H_2SO_4 following alternating cycles of N_2 and H_2. CPD measurements show noticeable differences in the CPD values of the pristine NP following the initial exposure to H_2 (Fig. 6a). Quantitative analysis of the CPD signal shows that

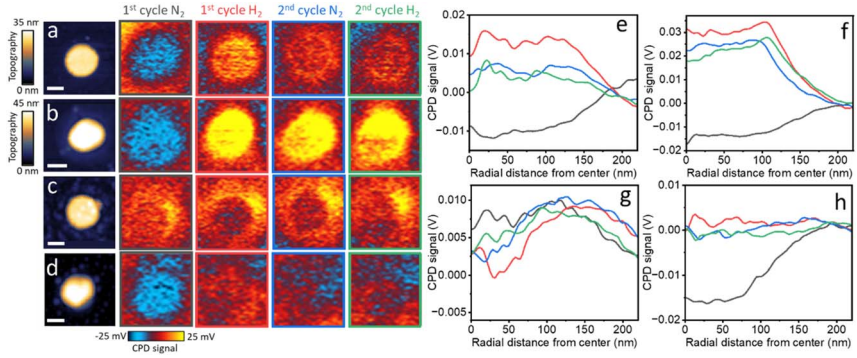

Fig. 6 AFM topography and KPFM of the pristine (a and c) and annealed (b and d) Pd NPs. Measurements were performed before (a and b, respectively) and after H_2SO_4 poisoning (c and d, respectively), following consecutive exposure to N_2 and H_2. The radial CPD signal analysis for the pristine (e and f) and annealed (g and h) NPs before (e and g) and after (f and h) H_2SO_4 poisoning are shown. CPD analysis is shown after the first exposure to N_2 and H_2 (black and red traces, respectively) and after the second exposure to N_2 and H_2 (blue and green traces, respectively). Scale bar represents 200 nm.

the CPD values at the center of the NP increased by ~25 mV after the initial exposure to H_2 (red colored curve, Fig. 6e). In the second N_2 and H_2 exposure cycle relatively minor changes were probed in CPD values. Interestingly, the CPD values at the rim of the NP showed a higher signal than at the center of the NP, demonstrating the high reactivity and affinity of hydrogen to these sites.

The annealed NP displayed noticeable changes in CPD values of up to 40 mV following H_2 exposure (Fig. 6b and red colored curve in Fig. 6f), indicative of enhanced hydrogen sorption affinity, correlated to improved crystallinity that led to higher diffusivity of hydrogen in the NP. Local enhancement in CPD values was measured at the rim of the NP, correlated to the higher density of surface defects at these sites. For both the pristine and annealed NPs, smaller changes were probed in the second N_2–H_2 exposure cycle, in comparison to the first cycle, attributed to the slower kinetics in hydrogen desorption from the top layers of the NPs.

Following H_2SO_4 poisoning, the CPD values of the pristine NP showed noticeable differences of up to 10 mV between the rim and the center of the NP (Fig. 6c and red colored curve in Fig. 6g). The non-homogeneous CPD signal along the NP's rim reflects the structural variance and heterogeneity in SO_x adsorption pattern that changed the hydrogen sorption affinity. Nevertheless, although the adsorption of SO_x species is located at rim sites (Fig. 4a), the magnitude of response to H_2 exposure is much smaller compared to the non-poisoned pristine NPs (Fig. 6a). These results show the dominant effect of sulfate adsorption at rim sites on the overall hydrogen sorption affinity. In contrast, the annealed sample that was poisoned by SO_x showed a more homogeneous CPD distribution after the first H_2 exposure (Fig. 6d and h).

These trends are consistent with the AFM-IR mapping results (Fig. 5a). After the first H_2 exposure, the pristine NPs displayed IR signature on the rim of the NP and this IR signature was identified as well in the CPD analysis. The annealed Pd NPs maintained stable IR signatures across the surface until the second H_2

exposure (Fig. 5b), which promoted SO_x sorption. Therefore, the CPD values do not show the rim signal that was detected for the pristine NP and show a moderate response to the change in the N_2 to H_2 environment due to surface poisoning of the NP.

Conclusions

This work demonstrates how the structure of Pd NPs governs their chemical reactivity, hydrogen (de)sorption affinity, and susceptibility to sulfur poisoning. Pristine Pd NPs, characterized by rough, defect-rich surfaces and largely amorphous interiors, exhibit rapid adsorption and reduction of SO_x species during H_2 exposure. In contrast, thermal annealing produces crystalline Pd nanostructures with reduced defect densities, leading to more spatially and chemically uniform SO_x adsorption.

Nanoscale AFM-IR mapping reveals that SO_x species distribute and evolve differently on pristine and annealed NPs. Pristine particles show rapid depletion of SO_x from their centers and selective retention at their more defective rims. Annealed NPs exhibit more stable SO_x signatures, with desorption occurring only after two cycles of hydrogen exposure. These trends correlate with AFM-derived surface roughness measurements and KPFM results, both of which confirm the more pronounced effect of poisoning on the annealed NPs, correlated to the lower density of surface defects, which limits the dissociative adsorption of H_2, followed by reduction and desorption of the adsorbed SO_x species.

These results establish a direct link between nanoscale crystallinity, defect density, and sulfur poisoning dynamics in Pd NPs. Annealed NPs are characterized by structural robustness, which induces stronger sulfur adsorption sites, and quenches the hydrogen sorption affinity. In contrast, pristine NPs are characterized by a high density of surface defects, leading to weaker SO_x adsorption sites and improved hydrogen (de)sorption affinity, in comparison to the annealed NPs. These nanospectroscopic insights underscore the importance of structural control in designing durable Pd-based catalysts and hydrogen-responsive sensors, and highlights nanoscale spectroscopy as a powerful tool for correlating local structure with chemical functionality.

Conflicts of interest

There are no conflicts to declare.

Data availability

The datasets supporting this article, titled “Structure-controlled sulfur poisoning and hydrogen-induced regeneration in single Pd nanoparticles probed by nanospectroscopy” are openly available on Zenodo and can be accessed *via* the DOI: https://doi.org/10.5281/zenodo.17934083.

Acknowledgements

This research was supported by the Swedish Foundation for Strategic Research (SSF) and Israel’s Ministry of Innovation, Science, and Technology (MOST), grant

no. 4250, and received funding from the Swedish Foundation for Strategic Research project SIP21-0032 and the Competence Centre TechForH2 (AT, CL). The Competence Centre TechForH2 is hosted by Chalmers University of Technology and is financially supported by the Swedish Energy Agency (P2021-90268) and the member companies Volvo, Scania, Siemens Energy, GKN Aerospace, PowerCell, Oxeon, RISE, Stena Rederier AB, Johnson Matthey, and Insplorion. Part of this work was carried out at the Chalmers MC2 cleanroom facility (μFab).

References

1 B. Hammer and J. K. Nørskov, Theoretical Surface Science and Catalysis-Calculations and Concepts, *Adv. Catal.*, 2000, **45**, 71–129, DOI: 10.1016/S0360-0564(02)45013-4.
2 H. J. Freund and G. Pacchioni, Oxide Ultra-Thin Films on Metals: New Materials for the Design of Supported Metal Catalysts, *Chem. Soc. Rev.*, 2008, **37**(10), 2224–2242, DOI: 10.1039/b718768h.
3 G. A. Somorjai and Y. Li, *Introduction to Surface Chemistry and Catalysis*, 2nd edn, Wiley, 2010.
4 N. Nilius and H. J. Freund, Activating Nonreducible Oxides *via* Doping, *Acc. Chem. Res.*, 2015, **48**(5), 1532–1539, DOI: 10.1021/acs.accounts.5b00018.
5 L. Vattuone, L. Savio and M. Rocca, *Influence of Defects on Adsorption Model Studies with Stepped Surfaces*, Encyclopedia of Interfacial Chemistry, 2018, pp. 38–165, DOI: 10.1016/B978-0-12-409547-2.11461-1.
6 M. Carmiel-Kostan, S. Nijem, S. Dery, G. Horesh and E. Gross, Composition-Reactivity Correlations in Platinum-Cobalt Nanoporous Network as Catalyst for Hydrodeoxygenation of 5-Hydroxymethylfurfural, *J. Phys. Chem. C*, 2019, **123**(50), 30274–30282, DOI: 10.1021/acs.jpcc.9b07453.
7 L. Rikanati, H. Shema, T. Ben-Tzvi and E. Gross, Nanoimaging of Facet-Dependent Adsorption, Diffusion, and Reactivity of Surface Ligands on Au Nanocrystals, *Nano Lett.*, 2023, **23**(12), 5437–5444, DOI: 10.1021/acs.nanolett.3c00250.
8 B. Friedman, L. Giloni, O. M. Gazit and E. Gross, Nanoscale Chemical Imaging of Basic Sites Distribution on Catalytically Active Mg–Al Mixed Oxide Particles, *Chem. Biomed. Imaging*, 2025, **3**(8), 560–568, DOI: 10.1021/cbmi.5c00017.
9 M. Kostan-Carmiel, A. Theodoridis, H. R. Eisenberg, T. Stein, C. Langhammer and E. Gross, Nanoscale Analysis of Sulfur Poisoning Effects on Hydrogen Sorption in Single Pd Nanoparticles, *ACS Nano*, 2025, **19**(42), 36969–36981, DOI: 10.1021/acsnano.5c08917.
10 C. H. Bartholomew, Mechanisms of Catalyst Deactivation, *Appl. Catal., A*, 2001, **212**(1–2), 17–60, DOI: 10.1016/S0926-860X(00)00843-7.
11 B. Coq and F. Figueras, Structure–Activity Relationships in Catalysis by Metals: Some Aspects of Particle Size, Bimetallic and Supports Effects, *Coord. Chem. Rev.*, 1998, **178–180**, 1753–1783, DOI: 10.1016/S0010-8545(98)00058-7.
12 C. Vogt and B. M. Weckhuysen, The Concept of Active Site in Heterogeneous Catalysis, *Nat. Rev. Chem.*, 2022, **6**, 89–111, DOI: 10.1038/s41570-021-00340-y.
13 Y. Wen, F. Wang, J. Zhu, Q. Wen, X. Xia, J. Wen, C. Deng, J. H. Du, X. Ke, Z. Zhang, H. Guan, L. Nie, M. Wang, W. Hou, W. Li, W. Tang, W. Ding, J. Chen and L. Peng, Revealing the Structure-Activity Relationship of Pt_1/

CeO_2 with ^{17}O Solid-State NMR Spectroscopy and DFT Calculations, *Nat. Commun.*, 2025, **16**(1), 3537, DOI: 10.1038/s41467-025-58709-2.

14 E. P. George, D. Raabe and R. O. Ritchie, High-Entropy Alloys, *Nat. Rev. Mater.*, 2019, **4**, 515–534, DOI: 10.1038/s41578-019-0121-4.

15 M. Ibáñez, S. C. Boehme, R. Buonsanti, J. De Roo, D. J. Milliron, S. Ithurria, A. L. Rogach, A. Cabot, M. Yarema, B. M. Cossairt, P. Reiss, D. V. Talapin, L. Protesescu, Z. Hens, I. Infante, M. I. Bodnarchuk, X. Ye, Y. Wang, H. Zhang, E. Lhuillier, V. I. Klimov, H. Utzat, G. Rainò, C. R. Kagan, M. Cargnello, J. S. Son and M. V. Kovalenko, Prospects of Nanosciencewith Nanocrystals: 2025 Edition, *ACS Nano*, 2025, **19**(36), 31969–32051, DOI: 10.1021/acsnano.5c07838.

16 R. Narayanan and M. A. El-Sayed, Shape-Dependent Catalytic Activity of Platinum Nanoparticles in Colloidal Solution, *Nano Lett.*, 2004, **4**(7), 1343–1348, DOI: 10.1021/nl0495256.

17 F. Ma, S. L. Ma, K. W. Xu and P. K. Chu, Surface Stability of Platinum Nanoparticles Surrounded by High-Index Facets, *J. Phys. Chem. C*, 2008, **112**(9), 3247–3251, DOI: 10.1021/jp077324v.

18 C. Xiao, B. A. Lu, P. Xue, N. Tian, Z. Y. Zhou, X. Lin, W. F. Lin and S. G. Sun, High-Index-Facet- and High-Surface-Energy Nanocrystals of Metals and Metal Oxides as Highly Efficient Catalysts, *Joule*, 2020, **4**(12), 2562–2598, DOI: 10.1016/j.joule.2020.10.002.

19 Y. Kang, S. M. João, R. Lin, K. Liu, L. Zhu, J. Fu, W. C. Cheong, S. Lee, K. Frank, B. Nickel, M. Liu, J. Lischner and E. Cortés, Effect of Crystal Facets in Plasmonic Catalysis, *Nat. Commun.*, 2024, **15**(1), 3923, DOI: 10.1038/s41467-024-47994-y.

20 X. F. Yang, A. Wang, B. Qiao, J. Li, J. Liu and T. Zhang, Single-Atom Catalysts: A New Frontier in Heterogeneous Catalysis, *Acc. Chem. Res.*, 2013, **46**(8), 1740–1748, DOI: 10.1021/ar300361m.

21 J. A. Van Bokhoven and S. Vajda, Size Selected Clusters and Particles: From Physical Chemistry and Chemical Physics to Catalysis, *Phys. Chem. Chem. Phys.*, 2014, **16**(48), 26418–26420, DOI: 10.1039/c4cp90163k.

22 I. Darmadi, F. A. A. Nugroho and C. Langhammer, High-Performance Nanostructured Palladium-Based Hydrogen Sensors – Current Limitations and Strategies for Their Mitigation, *ACS Sens.*, 2020, **5**(11), 3306–3327, DOI: 10.1021/acssensors.0c02019.

23 Y. Hayashi, H. Yamazaki, K. Masunishi, T. Ikehashi, N. Nakamura and A. Kojima, Effects of Poisoning Gases on and Restoration of PdCuSi Metallic Glass in a Capacitive MEMS Hydrogen Sensor, *Int. J. Hydrogen Energy*, 2020, **45**(1), 1187–1194, DOI: 10.1016/j.ijhydene.2019.10.245.

24 S. Zarabi Golkhatmi, M. I. Asghar and P. D. Lund, A Review on Solid Oxide Fuel Cell Durability: Latest Progress, Mechanisms, and Study Tools, *Renewable Sustainable Energy Rev.*, 2022, **161**, 112339, DOI: 10.1016/j.rser.2022.112339.

25 X. Xu, Y. Zhong, M. Wajrak, T. Bhatelia, S. P. Jiang and Z. Shao, Grain Boundary Engineering: An Emerging Pathway toward Efficient Electrocatalysis, *InfoMat*, 2024, **6**(8), e12608, DOI: 10.1002/inf2.12608.

26 H. Shooshtari Gugtapeh, A. H. Aghaii and A. Simchi, A Critical Review on the Role of Structural Defects in Electrochemical Nitrate Reduction Catalysts: From Mechanisms to Formation Strategies, *J. Environ. Chem. Eng.*, 2025, **13**(6), 120221, DOI: 10.1016/J.JECE.2025.120221.

27 A. Tittl, P. Mai, R. Taubert, D. Dregely, N. Liu and H. Giessen, Palladium-Based Plasmonic Perfect Absorber in the Visible Wavelength Range and Its Application to Hydrogen Sensing, *Nano Lett.*, 2011, **11**(10), 4366–4369, DOI: 10.1021/nl202489g.

28 C. Wadell, S. Syrenova and C. Langhammer, Plasmonic Hydrogen Sensing with Nanostructured Metal Hydrides, *ACS Nano*, 2014, **8**(12), 11925–11940, DOI: 10.1021/nn505804f.

29 R. Griessen, N. Strohfeldt and H. Giessen, Thermodynamics of the Hybrid Interaction of Hydrogen with Palladium Nanoparticles, *Nat. Mater.*, 2016, **15**(3), 311–317, DOI: 10.1038/nmat4480.

30 C. Andersson, J. Zimmerman, J. Fritzsche, E. Rabkin and C. Langhammer, Hydride Formation Pressures and Kinetics in Individual Pd Nanoparticles with Systematically Varied Levels of Plastic Deformation, *Nat. Commun.*, 2025, **16**(1), 9242, DOI: 10.1038/s41467-025-64311-3.

31 R. Delmelle, B. Amin-Ahmadi, M. Sinnaeve, H. Idrissi, T. Pardoen, D. Schryvers and J. Proost, Effect of Structural Defects on the Hydriding Kinetics of Nanocrystalline Pd Thin Films, *Int. J. Hydrogen Energy*, 2015, **40**(23), 7335–7347, DOI: 10.1016/J.IJHYDENE.2015.04.017.

32 S. Alekseeva, M. Strach, S. Nilsson, J. Fritzsche, V. P. Zhdanov and C. Langhammer, Grain-Growth Mediated Hydrogen Sorption Kinetics and Compensation Effect in Single Pd Nanoparticles, *Nat. Commun.*, 2021, **12**(1), 5427, DOI: 10.1038/s41467-021-25660-x.

33 X. Geng, S. Li, J. Heo, Y. Peng, W. Hu, Y. Liu, J. Huang, Y. Ren, D. Li, L. Zhang and L. Luo, Grain-Boundary-Rich Noble Metal Nanoparticle Assemblies: Synthesis, Characterization, and Reactivity, *Adv. Funct. Mater.*, 2022, **32**(34), 2204169, DOI: 10.1002/adfm.202204169.

34 N. J. J. Johnson, B. Lam, B. P. MacLeod, R. S. Sherbo, M. Moreno-Gonzalez, D. K. Fork and C. P. Berlinguette, Facets and Vertices Regulate Hydrogen Uptake and Release in Palladium Nanocrystals, *Nat. Mater.*, 2019, **18**(5), 454–458, DOI: 10.1038/s41563-019-0308-5.

35 J. Tang, S. Yamamoto, T. Koitaya, A. Yoshigoe, T. Tokunaga, K. Mukai, I. Matsuda and J. Yoshinobu, Mass Transport in the PdCu Phase Structures during Hydrogen Adsorption and Absorption Studied by XPS under Hydrogen Atmosphere, *Appl. Surf. Sci.*, 2019, **480**, 419–426, DOI: 10.1016/J.APSUSC.2019.02.180.

36 B. Ai, Y. Sun and Y. Zhao, Plasmonic Hydrogen Sensors, *Small*, 2022, **18**(25), 2107882, DOI: 10.1002/smll.202107882.

37 Z. Su, C. Zhang, X. Zhang, W. Chen, X. Zhang, S. Wang, Y. Yang and Z. Wang, Probe of Nanocatalysts In-Action by Ambient Pressure Photoelectron Spectroscopy, *Nano Res.*, 2025, **18**(9), 94907709, DOI: 10.26599/NR.2025.94907709.

38 Y. Mathieu, L. Tzanis, M. Soulard, J. Patarin, M. Vierling and M. Molière, Adsorption of SO_x by Oxide Materials: A Review, *Fuel Process. Technol.*, 2013, **114**, 81–100, DOI: 10.1016/J.FUPROC.2013.03.019.

39 Z. Say, M. Kaya, Ç. Kaderoğlu, Y. Koçak, K. E. Ercan, A. T. Sika-Nartey, A. Jalal, A. A. Turk, C. Langhammer, M. Jahangirzadeh Varjovi, E. Durgun and E. Ozensoy, Unraveling Molecular Fingerprints of Catalytic Sulfur Poisoning at the Nanometer Scale with Near-Field Infrared Spectroscopy, *J. Am. Chem. Soc.*, 2022, **144**(19), 8848–8860, DOI: 10.1021/jacs.2c03088.

40 X. Sun, J. Li, J. Fan, J. Fan, Q. Deng, M. Xu, H. Huang, J. Wu and D. Ye, Study on Sulfur-Resistant Pd-Based Catalysts for High-Efficiency Oxidation of VOCs, *J. Hazard. Mater.*, 2025, **491**, 137958, DOI: 10.1016/J.JHAZMAT.2025.137958.
41 W. Xu, J. S. Kong, Y.-T. E. Yeh and P. Chen, Single-Molecule Nanocatalysis Reveals Heterogeneous Reaction Pathways and Catalytic Dynamics, *Nat. Mater.*, 2008, 7(12), 992–996, DOI: 10.1038/nmat2319.
42 J. I. J. Choi, T.-S. Kim, D. Kim, S. W. Lee and J. Y. Park, Operando Surface Characterization on Catalytic and Energy Materials from Single Crystals to Nanoparticles, *ACS Nano*, 2020, **14**(12), 16392–16413, DOI: 10.1021/acsnano.0c07549.
43 I. M. N. Groot, Investigation of Active Catalysts at Work, *Acc. Chem. Res.*, 2021, **54**(23), 4334–4341, DOI: 10.1021/acs.accounts.1c00429.
44 O. M. Busch, W. Brijoux, S. Thomson and F. Schüth, Spatially Resolving Infrared Spectroscopy for Parallelized Characterization of Acid Sites of Catalysts *via* Pyridine Sorption: Possibilities and Limitations, *J. Catal.*, 2004, **222**(1), 174–179, DOI: 10.1016/J.JCAT.2003.11.002.
45 M. B. J. Roeffaers, G. De Cremer, J. Libeert, R. Ameloot, P. Dedecker, A. J. Bons, M. Bückins, J. A. Martens, B. F. Sels, D. E. De Vos and J. Hofkens, Super-Resolution Reactivity Mapping of Nanostructured Catalyst Particles, *Angew. Chem., Int. Ed.*, 2009, **48**(49), 9285–9289, DOI: 10.1002/anie.200904944.
46 M. A. Karreman, I. L. C. Buurmans, J. W. Geus, A. V. Agronskaia, J. Ruiz-Martínez, H. C. Gerritsen and B. M. Weckhuysen, Integrated Laser and Electron Microscopy Correlates Structure of Fluid Catalytic Cracking Particles to Brønsted Acidity, *Angew. Chem., Int. Ed.*, 2012, **51**(6), 1428–1431, DOI: 10.1002/anie.201106651.
47 J. Ruiz-Martínez, A. M. Beale, U. Deka, M. G. O'Brien, P. D. Quinn, J. F. W. Mosselmans and B. M. Weckhuysen, Correlating Metal Poisoning with Zeolite Deactivation in an Individual Catalyst Particle by Chemical and Phase-Sensitive X-Ray Microscopy, *Angew. Chem., Int. Ed.*, 2013, **52**(23), 5983–5987, DOI: 10.1002/anie.201210030.
48 C.-Y. Wu, W. J. Wolf, Y. Levartovsky, H. A. Bechtel, M. C. Martin, F. D. Toste and E. Gross, High-Spatial-Resolution Mapping of Catalytic Reactions on Single Particles, *Nature*, 2017, **541**(7638), 511–515, DOI: 10.1038/nature20795.
49 S. Dery, S. Kim, D. Haddad, A. Cossaro, A. Verdini, L. Floreano, F. D. Toste and E. Gross, Identifying Site-Dependent Reactivity in Oxidation Reactions on Single Pt Particles, *Chem. Sci.*, 2018, **9**(31), 6523–6531, DOI: 10.1039/C8SC01956H.
50 X. Mao, C. Liu, M. Hesari, N. Zou and P. Chen, Super-Resolution Imaging of Non-Fluorescent Reactions *via* Competition, *Nat. Chem.*, 2019, **11**(8), 687–694, DOI: 10.1038/s41557-019-0288-8.
51 Z. Li and D. Kurouski, Plasmon-Driven Chemistry on Mono- and Bimetallic Nanostructures, *Acc. Chem. Res.*, 2021, **54**(10), 2477–2487, DOI: 10.1021/acs.accounts.1c00093.
52 S. Dery, H. Mehlman, L. Hale, M. Carmiel-Kostan, R. Yemini, T. Ben-Tzvi, M. Noked, F. D. Toste and E. Gross, Site-Independent Hydrogenation Reactions on Oxide-Supported Au Nanoparticles Facilitated by Intraparticle Hydrogen Atom Diffusion, *ACS Catal.*, 2021, **11**(15), 9875–9884, DOI: 10.1021/acscatal.1c01987.

53 L. Rikanati, S. Dery and E. Gross, AFM-IR and s-SNOM-IR Measurements of Chemically Addressable Monolayers on Au Nanoparticles, *J. Chem. Phys.*, 2021, **155**(20), 204704, DOI: 10.1063/5.0072079.

54 S. Dery, B. Friedman, H. Shema and E. Gross, Mechanistic Insights Gained by High Spatial Resolution Reactivity Mapping of Homogeneous and Heterogeneous (Electro)Catalysts, *Chem. Rev.*, 2023, **123**(9), 6003–6038, DOI: 10.1021/acs.chemrev.2c00867.

55 A. Dazzi and C. B. Prater, AFM-IR: Technology and Applications in Nanoscale Infrared Spectroscopy and Chemical Imaging, *Chem. Rev.*, 2017, **117**(7), 5146–5173, DOI: 10.1021/acs.chemrev.6b00448.

56 D. Kurouski, A. Dazzi, R. Zenobi and A. Centrone, Infrared and Raman Chemical Imaging and Spectroscopy at the Nanoscale, *Chem. Soc. Rev.*, 2020, **49**(11), 3315–3347, DOI: 10.1039/C8CS00916C.

57 H. Fredriksson, Y. Alaverdyan, A. Dmitriev, C. Langhammer, D. S. Sutherland, M. Zäch and B. Kasemo, Hole–Mask Colloidal Lithography, *Adv. Mater.*, 2007, **19**(23), 4297–4302, DOI: 10.1002/adma.200700680.

58 N. Hoshi, M. Kuroda, T. Ogawa, O. Koga and Y. Hori, Infrared Reflection Absorption Spectroscopy of the Sulfuric Acid Anion Adsorbed on Pd(S)–[*n*(111) × (111)] Electrodes, *Langmuir*, 2004, **20**(12), 5066–5070, DOI: 10.1021/la036149g.

59 M. S. Wilburn and W. S. Epling, Formation and Decomposition of Sulfite and Sulfate Species on Pt/Pd Catalysts: An SO_2 Oxidation and Sulfur Exposure Study, *ACS Catal.*, 2019, **9**(1), 640–648, DOI: 10.1021/acscatal.8b03529.

60 A. B. Horn and K. Jessica Sully, ATR-IR Spectroscopic Studies of the Formation of Sulfuric Acid and Sulfuric Acid Monohydrate Films, *Phys. Chem. Chem. Phys.*, 1999, **1**(16), 3801–3806, DOI: 10.1039/A904544I.